

Processing and Mechanical Properties of Boron Carbide Sintered with TiC

L. S. Sigl

Elektroschmelzwerk Kempten GmbH, 87437 Kempten, Germany

(Received 27 October 1997; accepted 16 February 1998)

Abstract

The suitability of TiC as a sintering aid for boron carbide is investigated. The in situ reaction of TiC with boron carbide generates elemental carbon and TiB₂ which both aid the sintering process and permit pressureless sintering at temperatures between 2150 and 2200°C. Relative densities of as-sintered materials exceed 93% of theoretical, but can be increased to nearly full density by subsequent hot isostatic pressing. The grain size of both B₄C and TiB₂ increases with sintering temperature and decreases with the amount of sintering aid. The presence of TiB₂ causes a slight increase in Young's modulus and a small decrease of hardness as compared to single phase B₄C materials. The flexural strength of B₄C–TiC is found to decline with increasing fracture toughness. This behavior is related to crack length dependent toughness, particularly to the slope and steady state value of the R-curve. The dependence of R-curve properties on the grain size of the B₄C matrix is discussed. © 1998 Elsevier Science Limited. All rights reserved

1 Introduction

The pressureless densification of nonoxide ceramics such as SiC, Si₃N₄ or B₄C is difficult to achieve in pure materials. This behavior originates from the highly covalent bonding and the associated slow diffusion in such compounds. Suitable sintering aids have therefore been sought and various elements and compounds including AlF₃, Be₂C, TiB₂, W₂B₅, SiC, Al, Mg, Ni, Fe, Cu, Si and elemental carbon were proposed to aid the pressureless consolidation of boron carbide.^{1–13} Being most effective, carbon superseded all competitors and is now the standard additive for the densification of B₄C on an industrial scale. The knowledge of den-

sifying B₄C, accumulated in the seventies and eighties, discloses that a few per cent of elemental carbon added to submicrometer powder enhances sintering most effectively such that bodies with relative densities > 95% of the theoretical limit can be achieved.^{3–9}

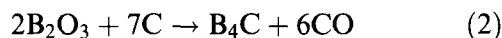
It is generally agreed that oxygen contaminants limit the densification of boron carbide, specifically boric oxide which forms a thin layer on the surface of B₄C powder particles.^{5–7} In combination with boron carbide, both B₂O₃ and excess oxygen in the sintering atmosphere, can generate suboxides, as illustrated by the gross reactions⁶



Being volatile, boron suboxides are effective in transporting boron and carbon through the vapor phase according to reaction eqn (1). Unfortunately, vapour phase transport merely redistributes matter to the necks between sintering powder particles rather than promoting a grain center approach which is mandatory for shrinkage. Specifically, vapor transport in B₄C was shown to coarsen the microstructure and by doing so, to reduce the driving force for sintering and to increase the average diffusion distance.^{6,7}

A primary aspect to be considered when sintering powder compacts to full density is a low grain boundary to surface energy ratio, as manifested by high dihedral angles.¹⁴ Complying with this condition is essential in energetically unfavorable configurations, e.g. for highly co-ordinated pores.^{14–17} Dole, who analysed partially sintered boron carbide powder networks, showed that oxygen-free grain clusters exhibit a dihedral angle of the order

120°.⁶ Thus densification of boron carbide is spontaneous, provided the detrimental role of boric oxide can be suppressed. A most suitable process for eliminating boric oxide is the reaction



Neglecting the pressure dependence of reaction eqn (2), the standard Gibbs Free Energy, ΔG^0 , suggests that desoxidation according to eqn (2) can roughly set in above 1300°C (Fig. 1), i.e. significantly below the onset of sintering.

Phenol-formaldehyde resins have until recently been the standard substance to introduce carbon into B_4C powders.⁵ Being pyrolyzed at temperatures above 600°C, the resins leave a thin layer of amorphous carbon on the powder-surface which subsequently removes B_2O_3 according to eqn (2). Though sintering proceeds very satisfactory, the resin-route suffers from serious drawbacks with respect to requirements of industrial processing. The handicaps include:

- polymerisation reactions in the resin which produce hard agglomerates;
- insufficient flow behavior of granules into pressing dies; and
- environmental problems caused by pyrolysis products.

These difficulties have driven the search for favorable substitutes. Only recently, the direct blending of B_4C with amorphous carbon was investigated and found to produce well sinterable powders.¹⁹ Nevertheless, homogeneous distribution of ultra-fine carbon in a B_4C slurry is a delicate process, and when done improperly, can lead to insufficient densities after sintering.

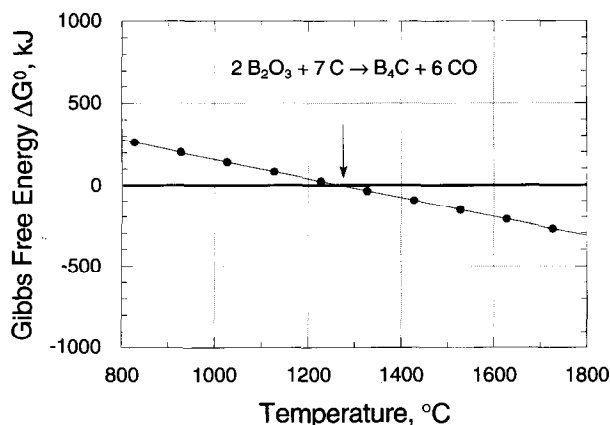


Fig. 1. The standard Gibbs free energy, ΔG^0 , of reaction (2) $2\text{B}_2\text{O}_3 + 7\text{C} \rightarrow \text{B}_4\text{C} + 6\text{CO}$. The thermodynamic data were obtained from Ref. 18.

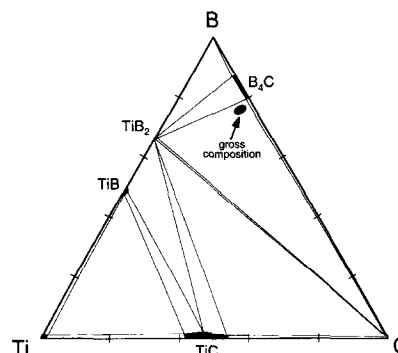
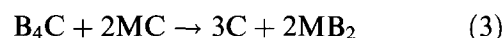


Fig. 2. Isothermal section of Ti-B-C phase diagram at 2000°C according to Rudy.²⁰

An as yet unexplored way of introducing elemental carbon into B_4C powders is opened by the incompatibility of transition metal carbides and boron carbide. The reactivity between B_4C and carbides of the MC-type, where M denotes a transition metal of groups IV-VI, is readily ascertained from the Ti-B-C phase diagram (Fig. 2²⁰). Mixtures of B_4C and MC react according to the stoichiometry



to form elemental carbon and a metal diboride. The standard Gibbs Free Energy of reaction eqn (3) is insensitive to the MC compound involved and assumes $\Delta G^0 \approx -200$ kJ/mol B_4C ,¹⁸ fairly independent of temperature. TiC as a sintering aid for B_4C was investigated in an earlier paper by Telle and Petzow.¹⁰ The role of TiC was, however, restrained to the formation of TiB_2 , because the free carbon on the right hand side of eqn (3) was deliberately bonded as B_4C by adding an appropriate amount of elemental boron.

The most striking advantage associated with the processing of MC sintering aids is their chemical similarity to boron carbide. Thus, unlike resins or amorphous carbon, metal carbides exhibit significantly less problems with long-term stability, dispersability of the sintering agent, or flow-behavior of spray-dried granules into die cavities. A particularly attractive carbide is TiC, because, in addition to the advantages described above, it is available at low cost. Furthermore, the *in situ* synthesized TiB_2 is anticipated to support sintering similar to the beneficial effects that have been observed in SiC-TiB_2 or $\text{B}_4\text{C-TiB}_2$ composites.^{10,12,13,21} Based on these considerations, the present research was initiated (i) to examine the potential of TiC as a sintering aid for B_4C and (ii) to assess the mechanical properties of $\text{B}_4\text{C-TiC}$ materials.

Table 1. Composition of raw materials

Mat.	BET m ² /g	FSSS μm	Free C wt%	O wt%	N wt%
B ₄ C	15.0	—	0.64	0.98	0.32
TiC	—	1.5	0.07	0.53	0.10

2 Experimental Procedures

Submicron boron carbide powder* (Table 1) was doped with various amounts of fine TiC[†] (Table 1) to yield samples with nominal contents of 1.5, 3, 4.5 and 6 wt% elemental carbon according to reaction eqn (1)[‡] (Table 2). The amount of TiC required for blending was determined from the stoichiometry of reaction eqn (3), taking into account that (i) 0.64 wt% elemental carbon is already present in the boron carbide starting powder (Table 1), and (ii) boron carbide solid solutions assume the composition B₁₃C₃ in the presence of elemental carbon.²² The B₄C–TiC blends were subsequently homogenized with water in a planetary ball mill for 1 h using boron carbide media and containers. After milling, the slurry was screened and freeze-dried. Bodies (60×20×20 mm³) were then formed by cold-isostatic pressing at 200 MPa. The specimens were eventually placed into a graphite tube sintering furnace and subjected to a two stage firing process. The B₄C–TiC reaction eqn (3) took place in a 60 min holding step at 1250°C. Further heat-up to sintering temperature was performed at 15°C/min. The specimens were finally held in a 10 mbar Ar-atmosphere for 2 h at various temperatures (2125, 2150, 2175 and 2200°C). The density of all specimens was determined by the water immersion method. Samples with closed porosity were further densified in a post-HIP cycle at 2050°C (30 min, 200 MPa Ar).

Table 2. Starting compositions, calculated composition assuming complete reaction and crystalline phases in sintered bodies

Alloy no.	TiC ^a wt%	B ₄ C ^a wt%	Elemental C ^b wt%	TiB ₂ ^b vol%	Crystalline phases
BTC 1.5	4.7	95.3	1.5	3.1	B ₄ C, TiB ₂ , graphite (trace)
BTC 3.0	8.9	91.1	3.0	6.1	B ₄ C, TiB ₂ , graphite
BTC 4.5	12.7	87.3	4.5	8.3	B ₄ C, TiB ₂ , graphite
BTC 6.0	16.5	83.5	6.0	10.9	B ₄ C, TiB ₂ , graphite

^aStarting composition.

^bNominal composition according to reaction (3).

*B₄C Tetrabor, ESK GmbH, Munich, Germany.

[†]TiC Grade B, H. C. Starck GmbH, Goslar, Germany.

[‡]These materials are denoted BTC followed by a number indicating the nominal carbon content in wt%.

From the flexure bars, samples were cut and polished by standard ceramographic methods to a 1 μm diamond paste finish. Some samples were electrolytically etched in 50% H₂SO₄ at 10 V. Polished and etched material was studied by optical and scanning electron microscopy. Each batch was subjected to microstructural characterization. The linear intercept technique was employed to measure the grain size with a semi-quantitative image analyser (Kontron Videoplan) being used to record and analyse the data. A total of at least 250 intercepts was counted per material. The hardness of as-sintered material was determined with a Leitz micro-hardness tester on as-polished surfaces with a Knoop diamond indenter using a load of 0.981 N (HK 0.1). Standard flexure bars (45×4.5×3.5 mm³) were cut from the post-HIPed bodies, ground and finally lapped. Young's modulus was calculated from vibration resonance spectra. A commercial unit (Förster Elastomat 1024) was used for recording the resonance data.

Pre-cracking of selected flexure specimens was performed with a modified bridge method,²³ which introduces naturally sharp flaws into the SENB bars. After pre-cracking, the crack front was marked by tinting with a fluorescent fluid, followed by a load rate controlled 4-pt bending test (loading rate 20 Ns⁻¹, outer span $S_2 = 40$ mm, inner span $S_1 = 20$ mm) where the fracture load, P , was recorded. The length of the precrack, c , was subsequently obtained as an average of five measurements over the crack front and fracture toughness, K_C , was eventually computed from

$$K_C = \frac{3}{2} P \frac{(S_2 - S_1)}{BW^2} \sqrt{c} Y\left(\frac{c}{W}\right) \quad (4)$$

where W and B denote the specimen width and height respectively and Y is a nondimensional stress intensity factor, valid in the interval $0 \leq c/W \leq 1$.²⁴ Since the fracture resistance of many ceramic materials grows during crack expansion (R -curve behavior), it is important to know which K -value on the R -curve actually obtains. A vast set of literature data suggests that toughness of engineering ceramics with growing cracking resistance saturates at cracking increments ≤ 2 mm.²⁵ Due to the large initial size of our precracks, i.e. $2.5 \leq c \leq 3$ mm, it is believed that the toughness data in Table 3 reflect the steady-state toughness (plateau toughness) rather than the rising part of the R -curve. The flexural strength of selected composites was determined in four-point bending using the toughness testing fixture at a loading rate of 20 Ns⁻¹ according to

Table 3. Mean strength and steady state toughness of sintered and post-HIPed BTC composites as a function of sintering temperature

Alloy no.	Flexural strength MPa			Steady state toughness MPa√m		
	2150°C	2175°C	2200°C	2150°C	2175°C	2200°C
BTC 1.5	292	286	266	4.2	4.0	3.7
BTC 3.0	368	n.d.	n.d.	3.6	n.d.	n.d.
BTC 4.5	454	n.d.	n.d.	3.2	n.d.	n.d.
BTC 6.0	502	n.d.	n.d.	2.9	n.d.	n.d.

n.d. = Not determined.

$$\sigma_f = \frac{3}{2} P \frac{(S_2 - S_1)}{BW^2} \quad (5)$$

Five specimens were fractured per material and the average strength was computed. Though the number of specimens is insufficient for performing a valid Weibull analysis, it is felt that the mean values supply sufficient information to discuss trends in strength properties.

3 Results and Discussion

3.1 Microstructure

Figure 3(a)–(d) shows representative microstructures of BTC materials sintered at 2150°C. It is noteworthy, that BTC 1.5 composites consist of a small fraction of pores, two major solid phases, i.e. TiB₂ grains in a B₄C matrix, and traces of a dark phase, which using polarised light and X-ray diffraction, is readily identified as graphite. Significantly more graphite becomes visible in the high carbon materials, i.e. in BTC 3.0, BTC 4.5 and BTC 6.0 (Table 2). Figure 3(c) and (d) shows that TiB₂ particles and graphite are in direct contact, indicating the simultaneous formation of both compounds consistent with reaction eqn (3). The precipitation of graphite is attributed to excess carbon that has not been used up for the desoxidation of B₄C particles according to reaction eqn (2). As expected, the amount of graphite and TiB₂ increases with the initial TiC content (c.f. Fig. 3).

The mean grain size of B₄C in all compositions is plotted in Fig. 4. As expected, there is a pronounced tendency for grain growth in B₄C with increasing sintering temperature.* However, the coarsening trend decreases with increasing amount of sintering aid as documented in Fig. 4. This plot, together with the observation that the number of second phase particles at grain boundaries increases with initial TiC content (Fig. 3), provides

*Post-HIPing does not increase the grain size, due to the low HIP temperature of 2050°C.

evidence that both TiB₂ and graphite precipitates are effective in pinning moving grain interfaces. Though not documented by quantitative image analysis, TiB₂ particles coarsen with increasing processing temperature as well. This coarsening happens most likely by coalescence,²⁶ a process which is aided by a remarkable solubility of 3 mol% TiB₂ in B₄C at the sintering temperature.²⁰ A typical feature associated with such diffusion controlled grain growth is the interconnection of TiB₂ grains across thin necks, viz. Fig. 3.

The size distribution of B₄C crystals is bimodal, i.e. it consists of a mixture of fine grains with a mean intercept length of $\approx 2\mu\text{m}$, and a second population of B₄C crystals which have already entered the regime of discontinuous growth. Though this feature is observed in all microstructures (Fig. 3), there is a trend that the volume fraction of discontinuous grains drops with increasing amount of initial TiC. Discontinuous B₄C grains typically show intragranular features, i.e. TiB₂ precipitates, graphite particles and pores which have been entrapped during grain growth. The number of these objects correlates inversely with the amount of initial TiC, viz. Fig. 3(a)–(d).

For reference purposes the grain size of B₄C doped with amorphous carbon¹⁹ is also included in Fig. 4. It is seen that higher sintering temperatures, which are needed in BTC materials to reach sufficient density, causes significantly more grain growth than in B₄C doped with amorphous carbon. One may speculate from this observation that graphite particles being introduced by ultra-fine amorphous carbon are smaller and hence more effective in retarding grain growth than graphite and TiB₂ generated from the reaction with TiC.

3.2 Sintering

The bulk densities of pressureless sintered composites are listed in Table 4. Relative densities were calculated assuming an ideal reaction according to eqn (3) and are plotted in Fig. 5 as a function of the sintering temperature. All compositions, except the 1.5 wt% carbon material, exceed a relative density of 95% at temperatures above 2150°C. In high carbon materials, density increases further as the sintering temperature is raised to 2200°C, whereas the density of materials with 1.5 and 3 wt% carbon declines at 2200°C. Composites

Table 4. Relative densities of BTC composites after sintering

Alloy no.	2100°C (%)	2125°C (%)	2150°C (%)	2175°C (%)	2200°C (%)
BTC 1.5	89.8	90.2	94.5	96.3	94.9
BTC 3.0	89.7	91.5	96.0	97.3	96.6
BTC 4.5	91.0	92.9	97.1	98.0	98.1
BTC 6.0	93.1	94.4	97.5	98.2	98.4

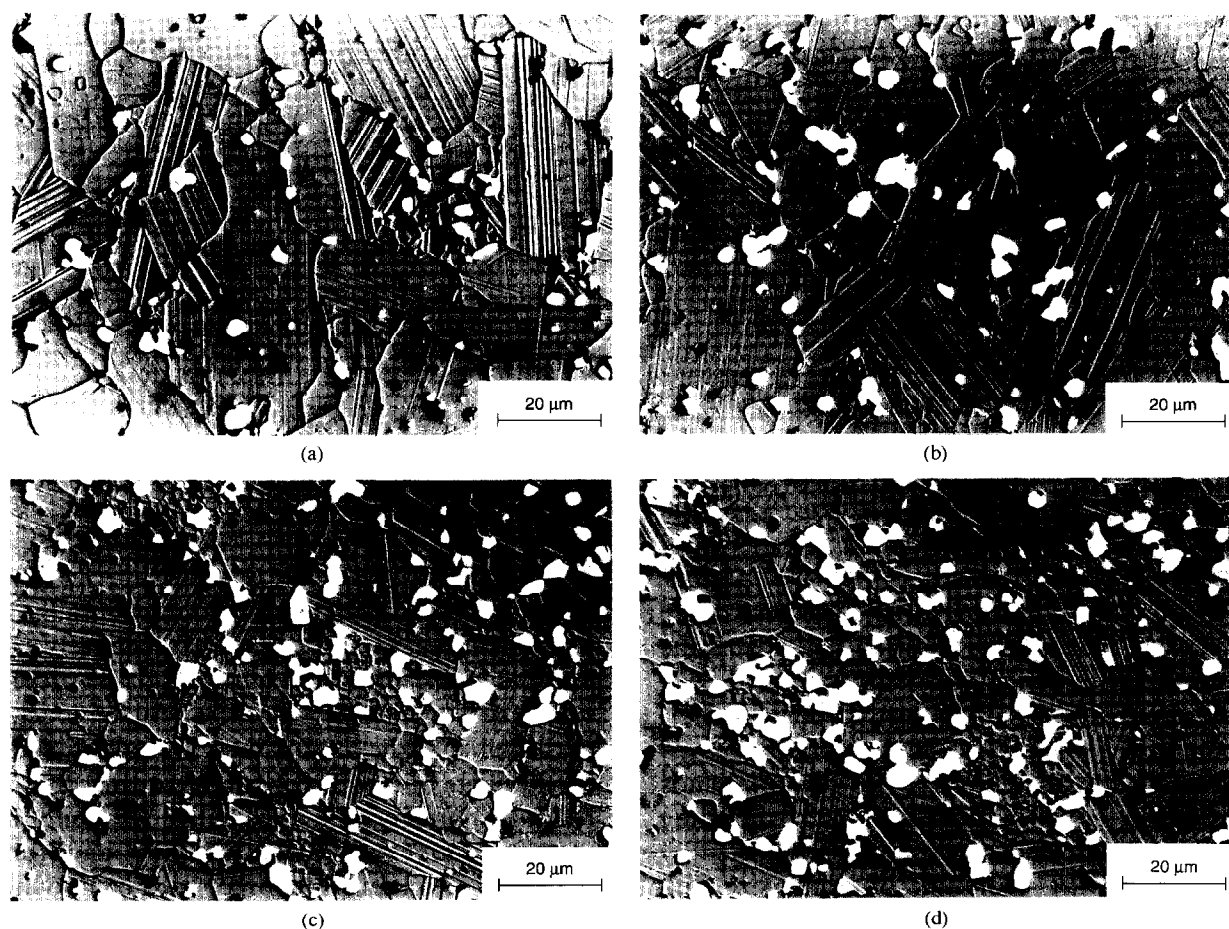


Fig. 3. Optical micrograph of B_4C -TiC sintered at 2150°C with a nominal carbon content of (a) 1.5 wt%, (b) 3 wt%, (c) 4.5 wt%, and (d) 6 wt%. The B_4C matrix is light grey, the arrows point at precipitates (white: TiB_2 , graphite: dark grey) which have formed according to reaction (3) and at pores (black). Note that graphite is virtually absent in BTC 1.5.

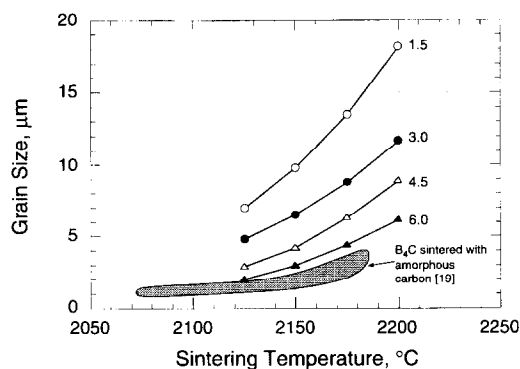


Fig. 4. Grain size of B_4C -TiC and of B_4C doped with amorphous carbon¹⁹ as a function of the sintering temperature. The labels indicate the nominal carbon content in wt%.

exceeding 95% of the theoretical density were post-HIPed and found to approach full density, virtually independent of the initial sintering temperature.

It is evident from Fig. 5 that the amount of TiC strongly affects densification behavior. Two effects must be distinguished:

1. Removal of B_2O_3 : Table 2 documents that graphite is present in all materials except BTC

1.5. Taking into account that the sintered bodies contain virtually no oxygen, a simple stoichiometric estimation can readily explain the absence of carbon in low-TiC materials. Reaction eqn (2) requires the mass fraction of carbon to be ≈ 1.75 times the initial oxygen mass fraction in the B_4C powder. Assuming that all oxygen is present as B_2O_3 , the initial oxygen content in the B_4C powder of 0.9 wt% (Table 1) would require 1.6 wt% elemental carbon for a complete reduction of B_2O_3 . The micrographs in Fig. 3 fully support this conclusion. Graphite is virtually absent in BTC 1.5, but begins to appear in BTC 3.0, and its fraction increases with rising TiC content. One may presume that, taking the inhomogeneous distribution of TiC into account, a minimum of ≈ 2 –3 wt% carbon is required to ensure that B_2O_3 is removed completely under conditions of routine processing. This conclusion is consistent with results reported by Refs 5 and 7, which also found that the density of B_4C with an initial oxygen content of ≈ 1 wt% becomes independent of the carbon addition above ≈ 3 wt% C.

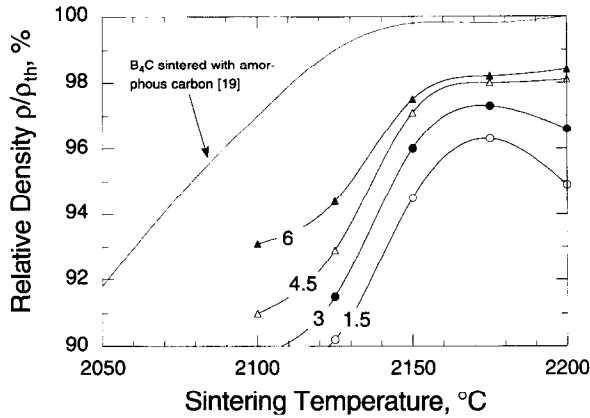


Fig. 5. Relative density of B_4C -TiC as a function of the sintering temperature. The density-temperature relation for B_4C doped with amorphous carbon¹⁹ has been included for comparison.

2. Retardation of grain growth by second phase particles: The density data in Fig. 5 and the grain growth behavior documented in Fig. 4 suggest that TiB_2 and excess carbon, in addition to the chemical effect of carbon, play a distinct role in sintering. Both compounds obviously enhance densification by retarding grain growth. This conclusion is supported by comparing the evolution of grain size and density at high sintering temperatures (Figs 4 and 5): while densities drop in composites, which provide only a small number of precipitates, i.e. in BTC 1.5 and 3.0, sintering in high carbon materials (BTC 4.5 and BTC 6.0) proceeds well even at higher temperatures. This behavior is readily ascertained from the micrographs in Fig. 3, which show that second phase precipitates located at grain boundaries limit the growth rate of B_4C crystals. A similar effect of sintering activity being improved by retardation of grain growth was recently observed in B_4C materials doped with amorphous carbon.¹⁹

3.3 Mechanical properties

The Young's modulus, E , of as-sintered material is plotted in Fig. 6 versus the volume fraction of TiB_2 . Also indicated are the lower and upper bounds for E using Paul's model²⁷ for series and parallel loading with E_{TiB_2} and E_{B_4C} taken as 440 GPa²⁸ and 540 GPa²⁹ respectively as determined for fully dense single phase B_4C and TiB_2 . The present data are somewhat below this simple prediction, most likely due to porosity and residual graphite.³⁰

Figure 7 shows a plot of the Knoop hardness of as-sintered material versus the TiB_2 volume fraction. Also included is a guideline which computes the hardness of B_4C - TiB_2 composites according to an 'inverse rule of mixtures' as suggested by

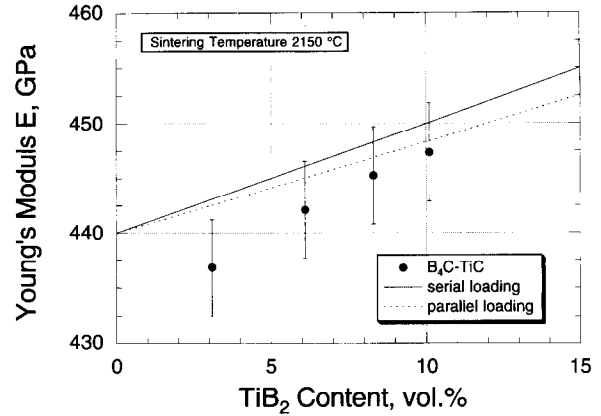


Fig. 6. Young's modulus of as-sintered materials as a function of TiB_2 content. Also indicated are the upper and lower bounds according to Paul's series and parallel loading model.²⁷

Warren,³¹ with the hardness of fully dense B_4C and TiB_2 taken as 34 and 26 GPa, respectively.³² The experimentally measured hardness of BTC composites differs by 5–10% from this simple model. The deviation may be rationalised by taking the soft constituents of the microstructure into account, i.e. residual porosity and particulate graphite. Both phases do not contribute to hardness, and truncate the effective volume fraction of hard compounds to approximately ≈ 91 –95 vol%, depending on the sintering temperature and the initial amount of TiC*. Recalling the empirical relationship that a small volume fraction of porosity, p , decreases the bulk hardness by a factor $\exp(-\alpha p)$, where α is a constant of the order 2,³⁰ qualitative agreement between experimental results and the prediction of Warren's rule of mixtures is recognized (Fig. 7).

The range of strength and toughness in BTC composites is generally comparable to B_4C materials sintered on the resin route. Data for fracture toughness, K_c , and flexural strength, σ_f , are disclosed in Table 3 as a function of the nominal carbon content for selected BTC materials. Applying the elementary Griffith concept, one would expect the strength of materials with unique fracture toughness to scale as

$$\sigma_f = \frac{K_c}{\sqrt{c}} \frac{1}{Y} \quad (6)$$

An inverse trend becomes, however, evident from Fig. 8 where flexural strength is plotted versus steady state toughness: while σ_f increases with sintering temperature, K_c drops, constituting just the opposite correlation between strength and toughness that one would expect from eqn (6). In

*The volume fraction of soft constituents (pores, graphite) may be estimated from the data in Tables 2 and 4.

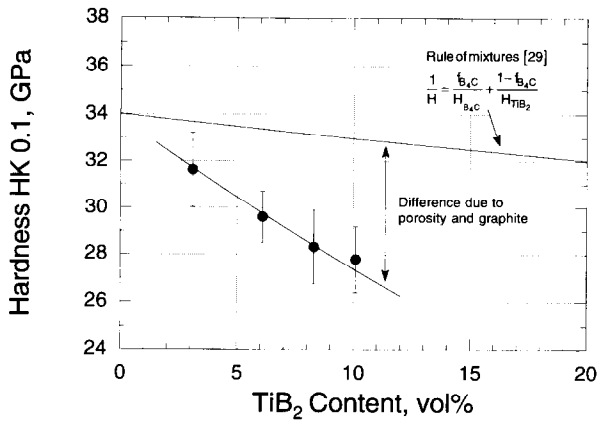


Fig. 7. Knoop hardness HK 0.1 of as-sintered materials as a function of TiB₂ content.

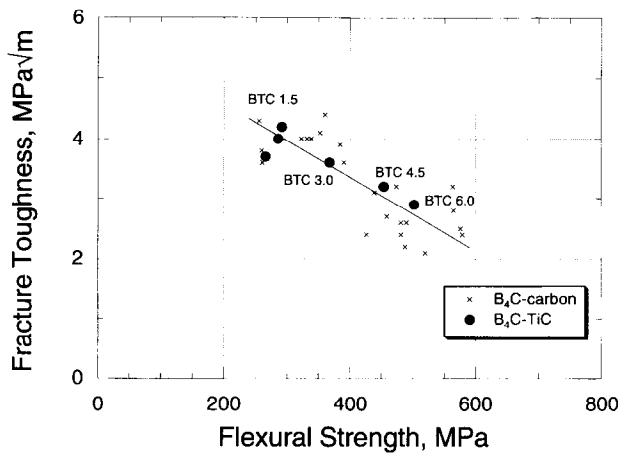


Fig. 8. Fracture toughness—strength relation of B₄C-TiC and of B₄C doped with amorphous carbon.

addition to the data for BTC materials, Fig. 8 also displays the toughness/strength relation of B₄C sintered with amorphous carbon. This plot reveals a general trend for the strength of boron carbide materials to drop with increasing steady state toughness. Similar toughness/strength characteristics have been observed in various ceramic materials, e.g. in alumina,³³ in Mg-PSZ and in Y-TZP materials,³⁴ and were interpreted in terms of crack length dependent toughness, the *R*- or *T*-curve.

Strength in brittle materials is controlled by the instability of a dominant critical flaw, i.e. by the conditions (1) $G > R$ and (2) $\partial G/\partial a > \partial R/\partial a$, where a is the flaw size, and G and R denote the energy release rate and fracture resistance respectively. Thus, non-unique toughness requires strength to be determined by the tangent construction outlined in Fig. 9,²⁵ rather than by applying the simplistic mechanics of eqn (6). In this context, it is important to recall a fundamental result of toughening in brittle materials: the slope of *R*-curves is generally inverse to the magnitude of the steady state toughness,³⁵ i.e. materials with gradual *R*-curves feature high steady state toughness (material No. 1 in Fig. 9) while steep *R*-curves are bound to low asymptotic fracture resistance

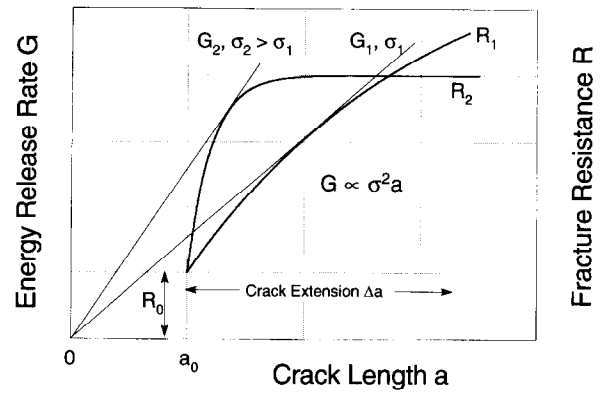


Fig. 9. Tangent method for determining strength in *R*-curve materials after Ref. 25.

(material No. 2 in Fig. 9). The instability condition $\partial G/\partial a < \partial R/\partial a$ then forces materials with high steady state toughness to fail at lower stresses than materials with low steady state toughness such that $\sigma_{f,1} < \sigma_{f,2}$ (Fig. 9). Thus the apparent strength in flexure drops, despite increasing steady state toughness. It should be noted, however, that this strength ranking is pertinent to *small* flaws, typical for flexure specimens, and may switch at large flaw sizes.

The fracture mechanics origin of the strength/toughness correlation in Fig. 8 being understood, it remains to rationalise the variation of steady state toughness. A closer look at the correlation between microstructure and mechanical properties is helpful to answer this question. Figure 10 shows a plot of the asymptotic fracture toughness of B₄C materials versus grain size. The fracture resistance data of BTC materials closely follow a scatter band, that is also characteristic for B₄C doped with amorphous carbon.³⁶ K_c starts at a toughness as low as 2 MPa√m, reflecting the inherent fracture resistance of B₄C, and increases up to a shallow maximum of ≈ 4 MPa√m at a grain size of about 10–15 μm, until K_c gradually drops again. An earlier study on the mechanical properties of boron

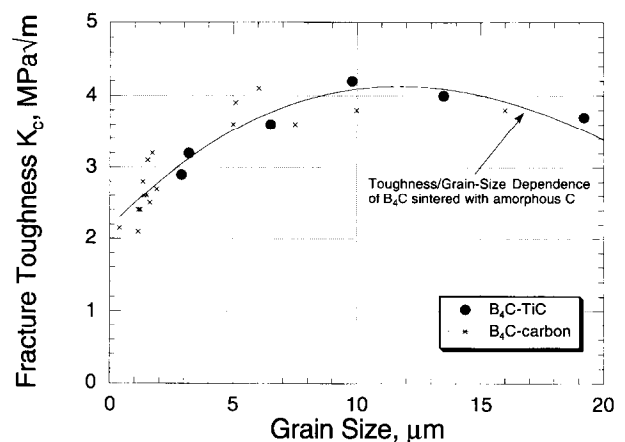


Fig. 10. Strength/grain size relationship of B₄C-TiC and B₄C doped with amorphous carbon.

carbide²⁹ demonstrated, that fracture switches continuously from inter- to transgranular cracking upon increasing grain size. Specifically, fracture in B_4C materials was observed to become predominantly transgranular at grain sizes $> 10 \mu\text{m}$.²⁹ Though specific fractography has yet not been performed, it is concluded that a similar transition threshold between trans- and intergranular fracture applies to BTC materials as well.

The toughness/grain-size relations in Fig. 10 are consistent with observations made in various ceramics, e.g. in alumina.³⁷ They have been interpreted in terms of interlocking grains which bridge the faces of a crack and generate a non-unique, crack length dependent fracture resistance.^{33,34,38} In this context it must be recalled that the steady state fracture resistance, R_{ss} , in materials with bridging zones is given by³⁵

$$R_{ss} = \int_0^{u_{\max}} p(u) d(u) \quad (7)$$

where u is the crack opening, u_{\max} is the opening at the end of the bridging zone and $p(u)$ is the bridging stress operating between the crack faces. Chantikul *et al.* have shown that the maximum pullout stress in grain bridging materials, $p(u)^{\max}$, remains virtually constant, i.e. is insensitive to changes in grain size.³³

The evolution of fracture resistance with grain size can then be argued as follows. At small grain sizes, fracture is fully intergranular. Though elastic and frictional bridges transmit tractions across the crack faces, steady state toughness is limited, because the grain size and hence the maximum pullout distance u_{\max} is still moderate. Increasing grain size enforces larger pullout distances, and according to eqn (7) augments the steady state toughness.^{33,39} However, as the microstructure becomes coarser, fracture increasingly would switch from an intergranular to a transgranular mode. Having less rough crack faces and hence shorter crack bridges, u_{\max} and consequently the steady state toughness will decline, giving rise to a maximum in the toughness grain size relation as shown in Fig. 10. Bearing the grain size sensitivity of steady state toughness in mind, it will be recalled that the slope of R -curves and the associated strength are affected accordingly.³⁵

Thus, it is concluded that the grain size controls the slope of the R -curve via the fracture mode and the associated bridging traction/crack opening function $p(u)$, and eventually enforces high flexural strength despite low steady state toughness. This trend is outlined in Fig. 11 which summarizes the

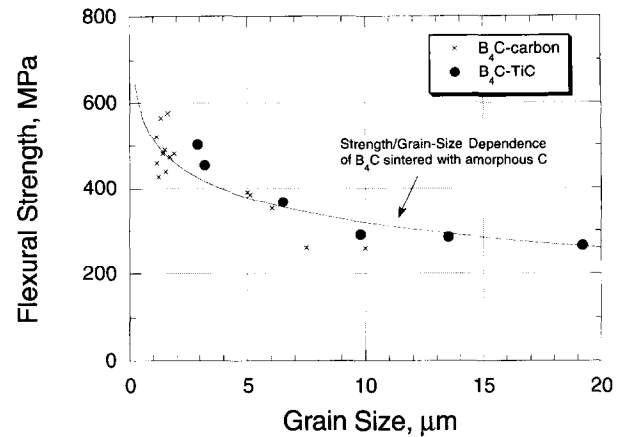


Fig. 11. Strength/grain size relationship of B_4C -TiC and B_4C doped with amorphous carbon.

dependence of flexural strength on grain size for B_4C materials doped both with TiC and amorphous carbon. As in many ceramic materials, the strength data could be fitted to a grain size dependence, where strength scales with the inverse square root of grain size, $D^{-1/2}$.³³ One should, however, bear in mind, that the origin of this behavior is non-unique toughness which must be *strictly* distinguished from the dislocation mechanism causing the 'Hall-Petch' $D^{-1/2}$ dependence of strength in metals.

4 Concluding Remarks

Titanium carbide happens to be to a useful additive for the pressureless consolidation of boron carbide. The hypothesis that carbon promotes sintering by deoxidising the powder surface according to reaction eqn (2) is consistent with the observation that graphite does not appear in the microstructure below nominal carbon levels of 1.5 wt%. Both carbon and TiB_2 which form during the reaction between TiC and B_4C obviously aid the sintering process by retarding grain growth. This directs the consolidation process towards sintering rather than coarsening of the microstructure.

It is also noteworthy that reasonable densification starts at temperatures comparable to resin doped materials, i.e. above 2150°C , but considerably later than when amorphous carbon is used as a sintering aid. The enhanced processing temperatures needed to sinter TiC materials enlarge the tendency for discontinuous grain growth and excess coarsening. This is suspected to be a major reason why, in contrast to materials sintered with amorphous carbon, microstructures with a grain size $\leq 2 \mu\text{m}$ cannot be preserved during sintering.

While hardness and elastic properties of BTC composites follow simple models, strength and toughness are triggered by a more complex

interaction between fracture resistance and grain size. This interaction leads to a non-unique toughness behavior characterized by a variability in both, slope of *R*-curves and steady state toughness. This relation finally causes strength to decrease with increasing grain size.

Acknowledgements

The author is indebted to H. Thaler and U. Napholz for their valuable assistance in conducting the sintering experiments and performing the ceramographic preparation.

References

1. Stibbs, D., Brown, C. and Thompson, R. *U.S. Patent*, 1973, 3,749,571.
2. Prochazka, S., *U.S. Patent*, 1977, 4,005,235.
3. Schwetz, K. A. and Vogt, G., *U.S. Patent*, 1980, 4,195,066.
4. Lange, R. G., Munir, Z. A. and Holt, J. B., Sintering kinetics of pure and doped boron carbide. In *Sintering Processes*, ed. G. C. Kuczynski. Plenum Press, New York, 1980, pp. 17–24.
5. Schwetz, K. A. and Grellner, W., The influence of carbon on the microstructure and mechanical properties of sintered boron carbide. *J. Less Common Metals*, 1981, **82**, 37.
6. Dole, S. L., Sintering of boron carbide, Ph.D. thesis, Rensselaer Polytechnic Institute, Troy NY, 1985.
7. Dole, S. L. and Prochazka, S., Densification and microstructure development in boron carbide. *Ceram. Eng. Sci. Proc.*, 1985, **6**, 1151–1160.
8. Thévenot, F. and Bougoin, M., Pressureless sintering of boron carbide phase. In *Boron Rich Solids*, ed. D. Emin, T. L. Aselage, C. L. Beckel, I. A. Howard and C. Wood. American Institute of Physics Conference Proceedings 140, New York, 1986, pp. 51–58.
9. Bougoin, M. and Thévenot, F., Pressureless sintering of boron carbide with an addition of polycarbosilane. *J. Mater. Sci.*, 1987, **22**, 109–114.
10. Telle, R. and Petzow, G., Reaction sintering of boron carbide with silicon and titanium. *Horiz. Powder Met.*, 1986, **2**, 1155–1158.
11. Zakhariyev, Z. and Radev, D., Properties of polycrystalline boron carbide sintered in the presence of tungsten boride (W_2B_5) without pressing. *J. Mat. Sci. Letters*, 1988, **7**, 695–696.
12. Kim, D. K. and Kim, C. H., Pressureless sintering and microstructural development of B_4C-TiB_2 composites. *Adv. Cer. Mater.*, 1988, **3**, 52–55.
13. Telle, R. and Petzow, G., Strengthening and toughening of boride and carbide hard material composites. *Mat. Sci. Eng.*, 1988, **A105/106**, 97–104.
14. Kingery, D. and Francois, B., The sintering of crystalline oxides, i. Interactions between grain boundaries and pores. In *Sintering and Related Phenomena*, ed. G. C. Kuczynski, N. A. Hooton and C. F. Gibson. Gordon and Breach, New York, 1967, pp. 471–498.
15. Lange, F. F., Sinterability of agglomerated powders. *J. Am. Cer. Soc.*, 1984, **67**, 83–89.
16. Kellett, B. and Lange, F. F., Thermodynamics of densification: I, sintering of simple particle arrays, equilibrium configurations, pore stability, and shrinkage. *J. Am. Cer. Soc.*, 1989, **72**, 725–734.
17. Prochazka, S., The role of boron and carbon in the sintering of silicon carbide. In *Proc. 6th Symp. on Special Ceramics*, ed. P. Popper. British Ceramics Research Association, Stoke-on-Trent, 1975, pp. 171–182.
18. JANAF. *Thermochemical Tables*, 2nd edn, NBS, Washington, DC, 1971.
19. Sigl, L. S. and Schwetz, K. A., Pressureless sintering of boron carbide with carbon black. In *Euro-Ceramics II*, Vol. 1, ed. G. Ziegler and H. Hausner. Deutsche Keramische Gesellschaft e. V., Köln, 1991, pp. 517–521.
20. Rudy, E., Ternary phase equilibria in transition metal–boron–carbon–silicon systems, Part V, Compendium of phase diagram data. U.S. Air Force Reports AF 33 (615)-1249 and AF 33 (615)-67-C-1513.
21. Sigl, L. S. and Kleebe, H. J., Microcracking in B_4C-TiB_2 composites. *J. Am. Cer. Soc.*, 1995, **78**, 2374–2380.
22. Schwetz, K. A. and Karduck, P., Investigations in the boron-carbon system with the aid of electron probe microanalysis. *J. Less Common Met.*, 1991, **175**, 1–11.
23. Warren, R. and Johannesson, B., Creation of stable cracks in hardmetals using bridge indentation. *Powd. Metall.*, 1984, **27**, 25–29.
24. Srawley, J. E. and Gross, B., In *Cracks and Fracture*, Am. Soc. Test. Mater. Spec. Tech. Publ. No. 601. American Society for Testing and Materials, Philadelphia, Pa., 1976, pp. 559–579.
25. Lawn, B. R., *Fracture of brittle solids*, 2nd edn, Cambridge University Press, Cambridge, 1993.
26. Ohya, Y., Hoffmann, M. J. and Petzow, G., Sintering of in situ synthesized SiC– TiB_2 composites with improved fracture toughness. *J. Am. Cer. Soc.*, 1992, **75**, 2479–2483.
27. Paul, B., Prediction of elastic constants of multiphase materials. *Trans. Metall. Soc. AIME*, 1960, **218**, 36–41.
28. Dorward, R. C., Indentation fracture of titanium diboride. *J. Mat. Sci. Letters*, 1985, **4**, 694–696.
29. Schwetz, K. A., Grellner, W. and Lipp, A., Mechanical properties of HIP treated sintered boron carbide. *Inst. Phys. Conf. Series*, 1984, **75**, 413–426.
30. Wu, C. M. and Rice, R. W., Porosity dependence of wear and other mechanical properties on fine-grained Al_2O_3 and B_4C . *Ceram. Eng. Sci. Proc.*, 1985, **6**, 977–994.
31. Warren, R., The indentation hardness of microstructures consisting of hard particles in a metallic matrix. In *4th Risø Int. Symp. on Metallurgy and Materials Science*, ed. J. B. Bilde-Sørensen, N. Hansen, A. Horswell, T. Leffers, H. Liholt, Risø National Laboratory, Roskilde, 1983, pp. 575–581.
32. Rice, R. W., Wu, C. M. and Borchelt, F., Hardness-grain size relations in ceramics. *J. Am. Cer. Soc.*, 1994, **77**, 2539–2553.
33. Chantikul, P., Bennison, S. J. and Lawn, B. R., Role of grain size in the strength and R-curve properties of alumina. *J. Am. Cer. Soc.*, 1990, **73**, 2419–2427.
34. Swain, M. V. and Rose, L. R. F., Strength limitations of transformation-toughened zirconia alloys. *J. Am. Cer. Soc.*, 1986, **69**, 511–518.
35. Evans, A. G., Perspective on the development of high-toughness ceramics. *J. Am. Cer. Soc.*, 1990, **73**, 187–206.
36. Sigl, L. S. unpublished research.
37. Mussler, B., Swain, M. V. and Claussen, N., Dependence of fracture toughness of alumina on grain size and test technique. *J. Am. Cer. Soc.*, 1982, **65**, 566–572.
38. Steinbrech, R. W., Knehans, R. and Schaarwächter, W., Increase of crack resistance during slow crack growth in Al_2O_3 bend specimens. *J. Mat. Sci.*, 1983, **18**, 265–270.
39. Mai, Y. W. and Lawn, B. R., Crack-interface grain bridging as a fracture resistance mechanism in ceramics: II; Theoretical fracture mechanics model. *J. Am. Cer. Soc.*, 1987, **70**, 289–294.